

LETTER TO THE EDITOR

# Study of the HCCNC and HNCCC isotopologs in TMC-1<sup>★</sup>

J. Cernicharo<sup>1</sup>, B. Tercero<sup>2,3</sup>, C. Cabezas<sup>1</sup>, M. Agúndez<sup>1</sup>, E. Roueff<sup>4</sup>, R. Fuentetaja<sup>1</sup>, N. Marcelino<sup>2,3</sup>, and P. de Vicente<sup>3</sup>

<sup>1</sup> Dept. de Astrofísica Molecular, Instituto de Física Fundamental (IFF-CSIC), C/ Serrano 121, 28006 Madrid, Spain.

e-mail: jose.cernicharo@csic.es, carlos.cabezas@csic.es

<sup>2</sup> Observatorio Astronómico Nacional (OAN, IGN), C/ Alfonso XII, 3, 28014, Madrid, Spain.

<sup>3</sup> Centro de Desarrollos Tecnológicos, Observatorio de Yebes (IGN), 19141 Yebes, Guadalajara, Spain.

<sup>4</sup> LERMA, Observatoire de Paris, PSL Research University, CNRS, Sorbonne Université, F-92190 Meudon (France)

Received; accepted

## ABSTRACT

We present the detection of the three <sup>13</sup>C isotopologs of HCCNC and HNCCC toward TMC-1 using the QUIJOTE line survey. In addition, the D species has also been detected for these two isomers of HCCCN, whereas the <sup>15</sup>N isotopolog was only detected for HCCNC. Using high-*J* lines of HCCNC and HNCCC, we were able to derive very precise rotational temperatures, column densities, and subsequently the isotopic abundance ratios. We found that <sup>12</sup>C/<sup>13</sup>C is ~90 for the three possible substitutions in both isomers. These results are slightly different from what has been found for the most abundant isomer HCCCN, for which abundances of 105, 95, and 66 were found for each one of the three possible positions of <sup>13</sup>C. The H/D abundance ratio was found to be 31±4 for HCCNC and of 53±6 for HNCCC. The latter is similar to the H/D abundance ratio derived for HCCCN (~59). The <sup>14</sup>N/<sup>15</sup>N isotopic abundance ratio in HCCNC is 243±24.

**Key words.** molecular data — line: identification — ISM: molecules — ISM: individual (TMC-1) — astrochemistry

## 1. Introduction

The ultra-sensitive line survey QUIJOTE<sup>1</sup> performed with the Yebes 40m radio telescope toward the prestellar cold core TMC-1 has enabled the unambiguous detection of near 50 molecules in the last three years (Cernicharo et al., 2021, 2023a, and references therein). The sensitivity of QUIJOTE is unprecedented, opening up new issues concerning the interpretation of the forest of unknown lines present in sensitive spectral sweeps. In addition to the detection of new molecular species, which is the main goal of the survey, we have to deal with the contribution of all isotopologs of any molecule producing line intensities larger than 50 mK. Additionally, we must also account for the presence of low-lying bending vibrational modes of abundant species (see the case of the  $\nu_{11}$  mode of C<sub>6</sub>H, Cernicharo et al., 2023a). One of the advantages of QUIJOTE is that it can provide a detection (for all isotopologs) of a molecule whose emission is optically thin, thereby permitting a direct estimation of the isotopic abundances of species containing C, O, S, N, and H.

The study of isotopic abundances as a function of the distance to the galactic center allows to trace stellar nucleosynthesis and constrain the chemical enrichment in our galaxy (see, e.g., Yan et al., 2023). Moreover, molecules are known to experience isotopic fractionation and this can be used to track the chemical evolution of molecular clouds and the transfer of chemical con-

tent to planetary systems (Ceccarelli et al., 2014). In this work, we report the detection and spectroscopic characterization of all isotopologs of HCCNC, along with the first detection in space and first spectroscopic characterization, of the <sup>13</sup>C isotopologs of HNCCC. The results presented here will allow us to improve the chemical models dealing with isotopic fractionation in molecular clouds (Roueff et al., 2015; Colzi et al., 2020; Loison et al., 2020; Sipilä et al., 2023). Although these models take into account <sup>13</sup>C and <sup>15</sup>N fractionation reactions with various degrees of approximation when including the dependence of the <sup>13</sup>C position and adopted reactions, none of them deal with isotopic exchange reactions involving HNCCC and HCCNC.

## 2. Observations

The observational data used in this work are part of QUIJOTE (Cernicharo et al., 2021), a spectral line survey of TMC-1 in the Q-band carried out with the Yebes 40m telescope at the position  $\alpha_{J2000} = 4^{\text{h}}41^{\text{m}}41.9^{\text{s}}$  and  $\delta_{J2000} = +25^{\circ}41'27.0''$ , corresponding to the cyanopolyynes peak (CP) in TMC-1. The receiver was built within the Nanocosmos project<sup>2</sup> and consists of two cold high-electron mobility transistor amplifiers covering the 31.0-50.3 GHz band with horizontal and vertical polarizations. Receiver temperatures achieved in the 2019 and 2020 runs vary from 22 K at 32 GHz to 42 K at 50 GHz. Some power adaptation in the down-conversion chains have reduced the receiver temperatures during 2021 to 16 K at 32 GHz and 30 K at 50 GHz. The backends are  $2 \times 8 \times 2.5$  GHz fast Fourier transform spectrometers with a spectral resolution of 38 kHz, providing the whole

<sup>★</sup> Based on observations carried out with the Yebes 40m telescope (projects 19A003, 20A014, 20D023, 21A011, 21D005 and 23A024). The 40m radio telescope at Yebes Observatory is operated by the Spanish Geographic Institute (IGN, Ministerio de Transportes, Movilidad y Agenda Urbana).

<sup>1</sup> Q-band Ultrasensitive Inspection Journey to the Obscure TMC-1 Environment

<sup>2</sup> <https://nanocosmos.iff.csic.es/>

coverage of the Q-band in both polarizations. A more detailed description of the system is given by Tercero et al. (2021).

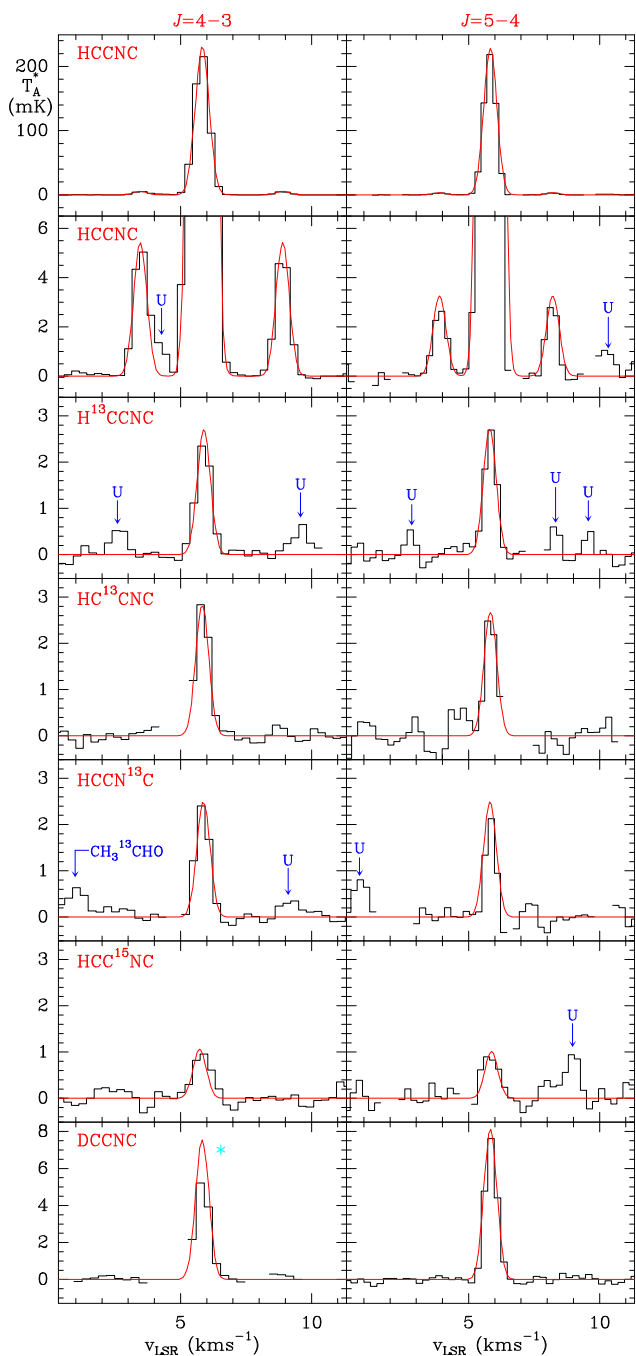


**Fig. 1.**  $J = 4 - 3$  and  $J = 5 - 4$  transitions of the single substituted isotopologs of HCCNC. The abscissa corresponds to the velocity with respect to the local standard of rest. The derived line parameters are given in Table A.1. The ordinate is the antenna temperature, corrected for atmospheric and telescope losses, in mK. Blanked channels correspond to negative features produced when folding the frequency-switched data. The red line shows the computed synthetic spectra for these lines (see Sect. 3.3). The second row panels correspond to a zoom in intensity of the lines of the main isotopolog (first row) to show the emission from its weak hyperfine components. The  $J=4-3$  line of DCCNC (marked with a cyan star) is affected by the negative features produced by the hyperfine structure of  $\text{CH}_3\text{CN}$  which is  $\sim 8$  MHz above in frequency.

The data of the QUIJOTE line survey presented here were gathered in several observing runs between November 2019

and July 2023. All observations are performed using frequency-switching observing mode with a frequency throw of 8 and 10 MHz. The total observing time on the source for data taken with frequency throws of 8 MHz and 10 MHz is 465 and 737 hours, respectively. Hence, the total observing time on source is 1202 hours. The measured sensitivity varies between 0.08 mK at 32 GHz and 0.2 mK at 49.5 GHz. The sensitivity of QUIJOTE is around 50 times better than that of previous line surveys in the Q band of TMC-1 (Kaifu et al., 2004). For each frequency throw, different local oscillator frequencies were used in order to remove possible side band effects in the down conversion chain. A detailed description of the QUIJOTE line survey is provided in Cernicharo et al. (2021). The data analysis procedure has been described by Cernicharo et al. (2022).

The main beam efficiency measured during our observations in 2022 varies from 0.66 at 32.4 GHz to 0.50 at 48.4 GHz (Tercero et al., 2021) and can be given across the Q-Band by  $B_{\text{eff}} = 0.797 \exp[-(\nu(\text{GHz})/71.1)^2]$ . The forward telescope efficiency is 0.97. The telescope beam size at half-power intensity is  $54.4''$  at 32.4 GHz and  $36.4''$  at 48.4 GHz.

Data for HCCNC and HNCCC in the millimeter domain have been taken with the IRAM 30m telescope and consist of a 3mm line survey that covers the full available band at the telescope, between 71.6 GHz and 117.6 GHz. The EMIR E0 receiver was connected to the Fourier transform spectrometers (FTS) in its narrow mode, which provide a spectral resolution of 49 kHz and a total bandwidth of 7.2 GHz per spectral setup. Observations were performed in several runs. Between January and May 2012, we completed the scan 82.5–117.6 GHz (Cernicharo et al., 2012). In August 2018, after the upgrade of the E090 receiver, we extended the survey down to 71.6 GHz. More recent high sensitivity observations in 2021 have been used to improve the signal to noise ratio (S/N) in several frequency windows (Agúndez et al., 2022; Cabezas et al., 2022). The final 3mm line survey has a sensitivity of 2–10 mK. However, at some selected frequencies, the sensitivity is as low as 0.6 mK. All the observations were performed using the frequency-switching method with a frequency throw of 7.14 MHz. The IRAM 30m beam varies between  $34''$  and  $21''$  at 72 GHz and 117 GHz, respectively, while the beam efficiency takes values of 0.83 and 0.78 at the same frequencies, following the relation:  $B_{\text{eff}} = 0.871 \exp[-(\nu(\text{GHz})/359)^2]$ . The forward efficiency at 3mm is 0.95.

The intensity scale utilized in this study is the antenna temperature ( $T_A^*$ ). The calibration was performed using two absorbers at different temperatures and the atmospheric transmission model ATM (Cernicharo, 1985; Pardo et al., 2001). The absolute calibration uncertainty is 10%. However, the relative calibration between lines within the QUIJOTE survey is certainly better as all them are observed simultaneously. The data were analyzed with the GILDAS package<sup>3</sup>.

### 3. Results

Line identification in this work has been performed using the MADEX code (Cernicharo, 2012), and the CDMS and JPL catalogues (Müller et al., 2005; Pickett et al., 1998). The references and laboratory data used by MADEX in its spectroscopic predictions are described below.

#### 3.1. Spectroscopy of HCCNC

HCCNC was detected toward TMC-1 by Kawaguchi et al. (1992a). The dipole moment is 2.93 D (Krüger et al., 1991),

<sup>3</sup> <http://www.iram.fr/IRAMFR/GILDAS>

which is lower than that of HCCCN. Guarnieri et al. (1992) observed rotational transitions of this species up to  $J_u=33$ . Hence, the rotational and distortion constants have been well established. However, the hyperfine structure was observed only for the  $J=1-0$  line (Krüger et al., 1992). The hyperfine structure of the  $J=4-3$  and  $J=5-4$  lines was observed toward TMC-1 with a previous version of the QUIJOTE line survey (Cernicharo et al., 2020). We remeasured the frequencies of these lines with the present QUIJOTE data (see Table A.1). In addition, the  $J=8-7$  up to  $J=11-10$  lines of HCCNC were observed with the IRAM 30m radio telescope. They are shown in Fig. A.1 and their line parameters are given in Table A.1. A fit to all the laboratory and space data was performed using the standard Hamiltonian of a linear molecule with a hyperfine structure. The results are given in Table 1. Therefore, the predictions for HCCNC, including the hyperfine structure, are reliable up to very high- $J$ . In addition, DCCNC was also observed in the laboratory up to  $J_u=51$  (Huckauf et al., 1998). The situation was completely different for the  $^{13}\text{C}$  and  $^{15}\text{N}$  isotopologs, for which only the  $J=1-0$  transition has been observed in the laboratory (Krüger et al., 1992). All these isotopologs were observed and characterized spectroscopically by Cernicharo et al. (2020), who observed their  $J=4-3$  and  $J=5-4$  transitions toward TMC-1. The present sensitivity of QUIJOTE is much better than that of 2020 and the frequency of the lines has been measured again in order to improve the rotational constants of these species. The observed lines of HCCNC,  $\text{H}^{13}\text{CCNC}$ ,  $\text{HC}^{13}\text{CNC}$ ,  $\text{HCCN}^{13}\text{C}$ ,  $\text{HCC}^{15}\text{NC}$ , and DCCNC are shown in Fig. 1 and their line parameters are given in Table A.1.

### 3.2. Spectroscopy of HNCCC

HNCCC was discovered in TMC-1 by Kawaguchi et al. (1992b) through the observation of three unknown lines in the Nobeyama spectral line survey of TMC-1 (Kaifu et al., 2004) that they assigned to this isomer of HCCCN. The dipole moment of this molecule has been computed through ab initio calculations to be 5.67 D (Botschwina et al., 1992). The molecule was observed in the laboratory by Hirahara et al. (1993) confirming the assignment of Kawaguchi et al. (1992b). These observations included the hyperfine components of the  $J=1-0$  and  $J=2-1$  transitions. Laboratory line frequencies up to  $J=31-30$  have been reported by Vastel et al. (2018). Several lines at 3mm have been also observed with our data gathered with the IRAM 30m radio telescope (see Fig. A.1). In addition, we have observed the hyperfine structure of the  $J=4-3$  and  $J=5-4$  lines with the QUIJOTE line survey (see Fig. 2). The derived line parameters for all observed transitions of HNCCC are given in Table A.1. All the spectroscopic data from the laboratory and our space observations were fitted with the same Hamiltonian than for HCCNC. The results are given in Table 1. Unlike the case of HCCNC, the only spectral information for the isotopologs of HNCCC concerns DNCCC (Hirahara et al., 1993). This isotopolog was observed in TMC-1 by Cernicharo et al. (2020). Improved frequencies for DNCCC are reported in Table A.1 and its derived rotational constants are given in Table 1. Assuming that the emission of HNCCC is not affected by line opacity, then we could expect to detect the lines from the  $^{13}\text{C}$  isotopologs at the level of 1-1.5 mK. For  $\text{H}^{15}\text{NCCC}$ , the same lines should be at the level of 0.5 mK (assuming the  $\text{HCCNC}/\text{HCC}^{15}\text{NC}$  abundance ratio). The expected molecular constants,  $B_0$  and  $D_0$ , of the isotopologs have been computed through ab initio calculations using  $B_{0,\text{exp}}(\text{HNCCC})/B_{e,\text{cal}}(\text{HNCCC})$  as the scaling factor. We estimated  $B_0 \sim 4655.5, 4644.0, 4501.0$ , and  $4545.4$  MHz for  $\text{HN}^{13}\text{CCC}$ ,  $\text{HNC}^{13}\text{CC}$ ,  $\text{HNCC}^{13}\text{C}$ , and  $\text{H}^{15}\text{NCCC}$ , respec-

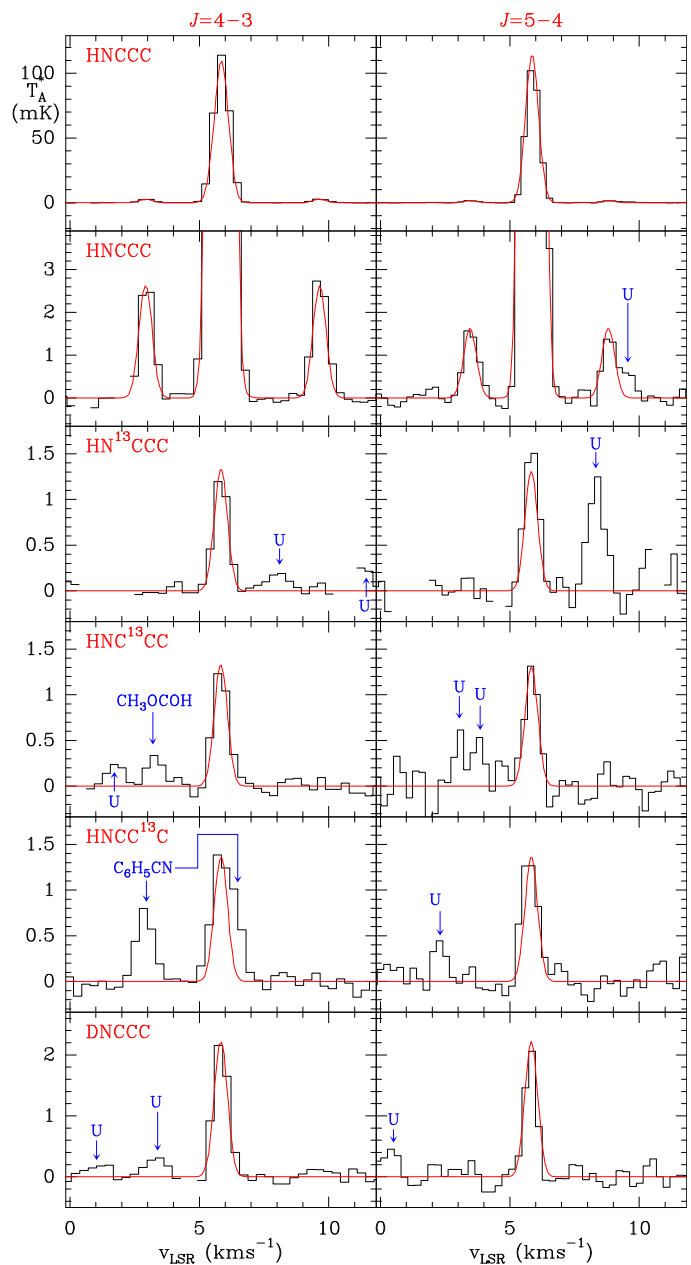


**Fig. 2.** Same as Fig. 1, but for HNCCC. The red line shows the computed synthetic spectra for these lines (see Sect. 3.3). The second row correspond to a zoom in intensity of the lines of the main isotopolog (first row). The derived line parameters are given in Table A.1.

tively. Three pairs of lines with similar intensities, as is the case for the isotopologs of HCCNC, have been easily found with a near perfect harmonic frequency relation 5/4 in our data close in frequency to our predictions. The deviation from this relation is  $3 \times 10^{-6}$  and fits the expected contribution of the distortion constant ( $\sim 0.6$  kHz). They correspond to the three  $^{13}\text{C}$  isotopologs and they are shown in Fig. 2. Their line parameters are given in Table A.1. As only two lines are available for each isotopolog, we have adopted a distortion constant of 0.61 kHz for  $\text{HN}^{13}\text{CCC}$  and  $\text{HNC}^{13}\text{CC}$ , and of 0.57 kHz for  $\text{HNCC}^{13}\text{C}$ . The derived rotational constants, for which we estimated a conservative uncertainty of 5 kHz, are given in Table 1. We have not been able to find a similar pair of lines that could be assigned to the  $^{15}\text{N}$  isotopolog because too many features do appear at the expected intensities of 0.5 mK. Thus, we report the first detection in space

**Table 1.** Derived rotational constants and column densities for the isotopologs of HCCNC and HNCCC

Species	$B$ (MHz)	$D$ (kHz)	$eQq$ (MHz)	$J_{max}$	$\sigma$ (kHz)	$N$ (cm $^{-2}$ )	Notes
HCCNC	4967.83827(12)	0.62694(14)	0.94628(81)	33	20.0	$(3.4\pm 0.10)\times 10^{12}$	A
H $^{13}$ CCNC	4813.11872(66)	0.559(41)	0.9429(39)	5	6.2	$(3.7\pm 0.15)\times 10^{10}$	B
HC $^{13}$ CNC	4949.44614(22)	0.605(14)	0.9457(13)	5	0.7	$(3.7\pm 0.15)\times 10^{10}$	B
HCCN $^{13}$ C	4804.87363(22)	0.555(13)	0.9447(12)	5	4.1	$(3.4\pm 0.15)\times 10^{10}$	B
HCC $^{15}$ NC	4944.73993(78)	0.516(33)		5	14.9	$(1.4\pm 0.15)\times 10^{10}$	B
DCCNC	4598.28896(03)	0.518(0)		51	3.3	$(1.1\pm 0.15)\times 10^{11}$	C
HNCCC	4668.33752(25)	0.62165(72)	1.0995(48)	31	19.9	$(5.8\pm 0.15)\times 10^{11}$	D
HN $^{13}$ CCC	4655.7452(50)	0.61		5	1.0	$(6.2\pm 0.20)\times 10^9$	E
HNC $^{13}$ CC	4643.5839(50)	0.61		5	1.0	$(6.2\pm 0.20)\times 10^9$	E
HNCC $^{13}$ C	4500.9332(50)	0.57		5	14.0	$(6.6\pm 0.20)\times 10^9$	E
DNCCC	4400.5916(50)	0.52	1.169(19)	5	22.3	$(1.1\pm 0.20)\times 10^{10}$	F

**Notes.** <sup>(A)</sup> Fit to the laboratory lines measured by Guarnieri et al. (1992) and Krüger et al. (1992), and to the hyperfine components of the  $J=4-3$  and  $5-4$  lines observed with QUIJOTE (see Table A.1). <sup>(B)</sup> Fit to the laboratory  $J=1-0$  hyperfine components measured by Krüger et al. (1992) and to the main component of the  $J=4-3$  and  $5-4$  lines observed with QUIJOTE (see Table A.1). <sup>(C)</sup> Fit to the laboratory lines measured by Huckauf et al. (1998). <sup>(D)</sup> Fit to the laboratory lines measured by Kawaguchi et al. (1992b), Hirahara et al. (1993), and Vastel et al. (2018). The hyperfine components of the  $J=4-3$  and  $5-4$  lines measured with QUIJOTE have been included in the fit. We have also added the frequencies of the  $J=8-7$ ,  $9-8$  and  $10-9$  lines measured with the IRAM 30m radio telescope (see Table A.1). The distortion constant  $H$  has been derived to be  $(1.57\pm 0.48)\times 10^{-9}$  MHz. Its inclusion in the fit reduces the standard deviation from 23.3 kHz to 19.9 kHz. <sup>(E)</sup> Fit to the two lines measured toward TMC-1. The distortion constant has been fixed for each isotopolog (see Sect. 3.2) and the uncertainty on  $B$  has been assumed to be 5 kHz. <sup>(F)</sup> Fit to the  $J=1-0$  and  $2-1$  lines measured by Hirahara et al. (1993) and to the  $J=4-3$  and  $5-4$  lines observed toward TMC-1 in this work.

**Table 2.** Isotopic abundance ratios

Species	$^{12}\text{C}/^{13}\text{C}_1$	$^{12}\text{C}/^{13}\text{C}_2$	$^{12}\text{C}/^{13}\text{C}_3$	H/D	N/ $^{15}\text{N}$
HCCNC	93 $\pm$ 6	93 $\pm$ 6	100 $\pm$ 7	31 $\pm$ 5	243 $\pm$ 24
HNCCC	94 $\pm$ 5	94 $\pm$ 5	88 $\pm$ 5	53 $\pm$ 6	
HCCNC <sup>A</sup>	106 $\pm$ 4	95 $\pm$ 2	69 $\pm$ 1	57 $\pm$ 2	317 $\pm$ 4

**Notes.** <sup>(A)</sup> From Tercero et al. (2024).

of the  $^{13}\text{C}$  isotopologs of HNCCC and the determination of their rotational constant.

### 3.3. Rotational temperatures and column densities

We analyzed the intensities of the lines of HCCNC and HNCCC using a rotational diagram to derive the rotational temperatures of these molecules. We assumed a source of uniform brightness temperature and a radius of 40'' (Fossé et al., 2001, Fuente-taja et al. 2023, in prep) to estimate the dilution factor for each transition. The line width adopted in the models to compute the synthetic spectra is  $0.6\text{ km s}^{-1}$  for all lines. The results of the rotational diagram for HCCNC are  $T_{rot}=5.5\pm 0.1\text{ K}$  and  $N=(3.4\pm 0.1)\times 10^{12}\text{ cm}^{-2}$ , while for HNCCC, we obtained  $T_{rot}=4.5\pm 0.2\text{ K}$  and  $N=(5.8\pm 0.2)\times 10^{11}\text{ cm}^{-2}$ . The corresponding synthetic spectra are shown in Fig. 1 for HCCNC and in Fig. 2 for HNCCC. We note that the weak hyperfine satellite lines of HCCNC and HNCCC are very well reproduced with the derived values for the column densities. These hyperfine components represent 2% and 1.3% of the total intensity of the  $J=4-3$  and  $5-4$  transitions, respectively. The fact that the modeled intensities for the weak and strong hyperfine components are in perfect agreement with the observations indicates that the emission of the  $J=4-3$  and  $5-4$  transitions of HCCNC. In addition, HNCCC is mostly optically thin. Hence, the derived column densities can be used to obtain isotopic abundance ratios. By adopting the rotational temperatures derived for HCCNC and HNCCC for all their isotopologs, we obtained the column densities given in Table 1. The match between computed and observed spectra is ex-

cellent (see Figures 1 and 2) and the derived isotopic abundance ratios are given in Table 2. We note that the synthetic spectra derived from the assumption of a constant rotational temperature reproduce the observed spectra at 3mm for both species rather well. Nevertheless, the column density of HNCCC has to be reduced by a factor 1.5 to reproduce the observed intensities of this species at 3mm.

Collisional rates for HCCNC and HNCCC with  $p\text{-H}_2$  and  $o\text{-H}_2$  have been calculated by Bop et al. (2021). We used the large velocity gradient approximation (LVG), described by Goldreich & Kwan (1974) and implemented in the MADEx code (Cernicharo, 2012), to model the line profiles of the  $J=4-3$  to  $J=11-10$  lines of both isomers. We explored the density and the column density that produce the best fit to the  $J=8-7$  to  $J=11-10$  lines of these species using  $p\text{-H}_2$  as collider. For HCCNC the best fit is obtained for  $n(\text{H}_2)=(7.0\pm 0.3)\times 10^3\text{ cm}^{-3}$  and  $N=(2.7\pm 0.2)\times 10^{12}\text{ cm}^{-2}$ . The excitation temperatures vary between 7.3 K for the  $J=4-3$  transition to 4.7 K for the  $J=11-10$  one. The generated synthetic spectra are shown in blue in Fig. A.1. These synthetic spectra agree rather well with those obtained for a constant rotational temperature of 5.5 K and  $N=3.4\times 10^{12}\text{ cm}^{-2}$  (synthetic spectra shown in red in Fig. A.1). However, this fit to the volume density and column density to the 3mm lines does not adequately reproduce the observations of the  $J=4-3$  and  $J=5-4$  lines. The differences between the two methods are probably related to the density structure of the source and to the accuracy of the collisional rates. We note that the derived density is lower than that derived from other molecules in TMC-1. We checked the effect of using  $o\text{-H}_2$  as collider and found similar results. In the case of HNCCC, our LVG calculations indicate that the intensity of the 3mm lines are well reproduced, with  $n(\text{H}_2)=1.5\times 10^4\text{ cm}^{-3}$  and a column density of  $3.8\times 10^{11}$ . The excitation temperatures vary between 5.6 K for the  $J=4-3$  transition to 4.0 K for the  $J=11-10$  one. The computed synthetic spectra are shown in blue in Fig. A.1 and agree well with those obtained from a constant rotational temperature (red curve in Fig. A.1). It is worth noting that in this case the derived volume density is in better agreement with the values derived from other species. We note also that

as for HCCNC, the best column density obtained from the LVG analysis is lower than that obtained by the rotational diagram. The most plausible explanation for these differences in both isomers is related to the cloud density structure, that is, the dense core of TMC-1 can not be treated as an object of uniform density. Moreover, it is also likely that molecular abundances vary across the core.

#### 4. Discussion

For the following discussion, we adopt the values derived above for the column densities using an uniform rotational temperature for all observed transitions. Taking the column density of HCCCN derived by Tercero et al. (2023, in prep.) of  $1.9 \times 10^{14} \text{ cm}^{-2}$ , the relative abundance ratios are 56, 328, and 6 for HCCCN/HCCNC, HCCCN/HNCCC, and HCCNC/HNCCC, respectively. These values agree, within a factor of two, with those obtained from less sensitive line surveys of TMC-1 (Gratier et al., 2016). The derived abundance for the isotopologs of HCCNC, HNCCC, and HCCCN permits us to study the isotopic  $^{12}\text{C}/^{13}\text{C}$  abundance ratio for the three possible substitutions. The results are given in Table 2. We found that for HCCNC and HNCCC this isotopic ratio does not depend on the substituted carbon, being very similar to the solar one and slightly larger than that of the local ISM of 59-76 (Lucas & Liszt, 1998; Wilson, 1999; Milam et al., 2005; Sheffer et al., 2007; Stahl et al., 2008; Ritchey et al., 2011). The results from Tercero et al. (2023, in prep) for HCCCN also indicate that for the most abundant isomer, the only isotopolog whose ratio is slightly different is  $\text{HCC}^{13}\text{CN}$ . Table 2 presents a summary of these ratios.

The  $^{13}\text{C}$  isotopic ratios derived for HCCCN in TMC-1 are in agreement with previous determinations in other cold dense clouds, such as L1521B, L134N (Taniguchi et al., 2017), L1527 (Yoshida et al., 2019), and L483 (Agúndez et al., 2019); more specifically,  $\text{HCC}^{13}\text{CN}$  is somewhat more abundant than the other two  $^{13}\text{C}$  isotopologs. The  $^{12}\text{C}/^{13}\text{C}$  ratio for  $\text{HCC}^{13}\text{CN}$  in TMC-1 is consistent with the local ISM  $^{12}\text{C}/^{13}\text{C}$  ratio, while the isotopologs  $\text{H}^{13}\text{CCCN}$  and  $\text{HC}^{13}\text{CCN}$  are somewhat diluted in  $^{13}\text{C}$ . This behavior is reproduced by the chemical model of Loison et al. (2020), assuming that  $\text{C}_3$  reacts with oxygen atoms, although we caution that there are uncertainties in some of the relevant chemical reactions. In the cases of HCCNC and HNCCC, the three  $^{13}\text{C}$  isotopologs show similar abundances, somewhat above the local ISM  $^{12}\text{C}/^{13}\text{C}$  ratio. A slight dilution in  $^{13}\text{C}$  was therefore found for the three isotopologs of HCCNC and HNCCC.

The dependence of the isotopic ratio between  $\text{HC}_3\text{N}$  and carbon substituted  $\text{HC}_3\text{N}$  on the position of the  $^{13}\text{C}$  was previously discussed by Taniguchi et al. (2016, 2017). They concluded that the main formation of  $\text{HC}_3\text{N}$  comes from the neutral-neutral reaction between acetylene  $\text{C}_2\text{H}_2$  and CN. The  $^{13}\text{C}$  substituted  $\text{HC}_3\text{N}$  has been considered in the fractionation models of Loison et al. (2020), who obtained a satisfactory agreement with observations when introducing a moderate value for the  $\text{C}_3$  and O reaction rate coefficient. The most recent paper by Sipilä et al. (2023) only introduces  $^{13}\text{C}$  fractionation reactions for CCH,  $\text{C}_3$ , and  $c\text{-C}_3\text{H}_2$ . The three  $^{13}\text{C}$  isotopomers of  $\text{HC}_3\text{N}$  thus have equal abundances over the full time dependence in the corresponding models.

The carbon and nitrogen isotopic chemistry of HCCNC and HNCCC has not seen very much interest until now and no chemical model has been performed to predict their isotopic ratios as yet. The deuterated species were detected by Cernicharo et al. (2020) and the abundance ratios were reported and modeled

in Cabezas et al. (2021) with reasonable success. Interestingly, the recent detection of  $\text{HCCNCH}^+$  by Agúndez et al. (2022), showing a high  $\text{HCCNCH}^+$  over HCCNC ratio (on the order of  $10^{-2}$ ), is surprisingly well reproduced in the associated chemical model. This is contrary to the results seen for most other protonated molecules. Following the KIDA database suggestion (Wakelam et al., 2012), we find that  $\text{HCCNCH}^+$  is efficiently formed through the  $\text{C}^+ + \text{CH}_3\text{CN}$  reaction that can return HCCNC through dissociative recombination amongst other products. This mechanism prevails over the other proton transfer reactions in our chemical model. Such an ion-molecule scheme may lead to different isotopic ratios than the neutral-neutral formation channels. Further studies on these topics are desirable to build on these results.

*Acknowledgements.* We thank Ministerio de Ciencia e Innovación of Spain (MICIU) for funding support through projects PID2019-106110GB-I00, PID2019-107115GB-C21 / AEI / 10.13039/501100011033, and PID2019-106235GB-I00. We also thank ERC for funding through grant ERC-2013-Syg-610256-NANOCOSMOS.

#### References

- Agúndez, M., Marcelino, N., Cernicharo, J., et al. 2019, *A&A*, 625, A147  
 Agúndez, M., Cabezas, C., Marcelino, N., et al. 2022, *A&A*, 659, L9  
 Bop, C.T., Lique, F., Faure, A., et al. 2021, *MNRAS*, 501, 1911  
 Botschwina, P., Horn, M., Seeger, S. & Flügge, J. 1992, *Chem. Phys. Lett.*, 195, 427  
 Cabezas, C., Roueff, E., Tercero, B. et al. 2021, *A&A*, 650, L15  
 Cabezas, C., Agúndez, M., Marcelino, N., et al. 2022, *A&A*, 657, L4  
 Ceccarelli, C., Caselli, P., Bockelée-Morvan, D., et al. 2014, in *Protostars and Planets VI*, eds. H. Beuther, R. S. Kiessen, C. P. Dullemond, and T. Henning, Univ. Arizona Press, 859  
 Cernicharo, J. 1985, Internal IRAM report (Granada: IRAM)  
 Cernicharo, J., 2012, in *ECLA 2011: Proc. of the European Conference on Laboratory Astrophysics*, EAS Publications Series, 2012, Ed.: C. Stehl, C. Joblin, & L. d'Hendecourt (Cambridge: Cambridge Univ. Press), 251; [https://nanocosmos.iff.csic.es/?page\\_id=1619](https://nanocosmos.iff.csic.es/?page_id=1619)  
 Cernicharo, J., Marcelino, N., Roueff, E., et al. 2012, *ApJ*, 759, L43  
 Cernicharo, J., Marcelino, N., Agúndez, M. et al. 2020, *A&A*, 642, L8  
 Cernicharo, J., Agúndez, M., Kaiser, R., et al. 2021, *A&A*, 652, L9  
 Cernicharo, J., Fuentetaja, R., Agúndez, M. et al. 2022, *A&A*, 663, L9  
 Cernicharo, J., Fuentetaja, R., Agúndez, M. et al. 2023a, *A&A*, 680, L4  
 Colzi, L., Sipilä, O., Roueff, E., et al. 2020, *A&A*, 640, A51  
 Fossé, D., Cernicharo, J., Gerin, M., Cox, P. 2001, *ApJ*, 552, 168  
 Goldreich, P. & Kwan, J. 1974, *ApJ*, 189, 441  
 Gratier, P., Majumdar, L., Ohishi, M. et al. 2016, *ApJS*, 225, 25  
 Guarnieri, A., Hinze, R., Krüger, M. & Zerbe-Feose, H. 1992, *J. Mol. Spectrosc.*, 156, 39  
 Hirahara, Y., Ohshima, Y. & Endo, Y. 1993, *ApJ*, 403, L83  
 Huckauf, A., Guarniere, A., Lentz, D. & Fayt, A. 1998, *J. Mol. Spectrosc.*, 188, 109  
 Kaifu, N., Ohishi, M., Kawaguchi, K., et al. 2004, *PASJ*, 56, 69  
 Kawaguchi, K., Ohishi, M., Ishikawa, S.-I. & Kaifu, N. 1992a, *ApJ*, 386, L51  
 Kawaguchi, K., Takano, S., Ohishi, M. et al. 1992b, *ApJ*, 396, L49  
 Krüger M., Dreizler, H., Preugschat, D. & Lentz, D. 1991, *Angew. Chem. Int. Ed. Engl.*, 30, 1644  
 Krüger M., Stahl W. & Dreizler, H. 1992, *J. Mol. Spectrosc.*, 158, 298  
 Loison, J.-C., Wakelam, V., Gratier, P., & Hickson, K. M. 2020, *MNRAS*, 498, 4663  
 Lucas, R. & Liszt, H. 1998, *A&A*, 337, 246  
 Milam, S. N., Savage, C., Brewster, M. A., & Ziurys, L. M. 2005, *ApJ*, 634, 1126  
 Müller, H. S. P., Schlöder, F., Stutzki, J., Winnewisser, G. 2005, *J. Mol. Struct.*, 742, 215  
 Pardo, J. R., Cernicharo, J., Serabyn, E. 2001, *IEEE Trans. Antennas and Propagation*, 49, 12  
 Pickett, H.M., Poynter, R. L., Cohen, E. A., et al. 1998, *J. Quant. Spectrosc. Radiat. Transfer*, 60, 883  
 Ritchey, A. M., Federman, S. R., & Lambert, D. L. 2011, *ApJ*, 728, 36  
 Roueff, E., Loison, J.-C., & Hickson, K. M. 2015, *A&A*, 576, A99  
 Sheffer, Y., Rogers, M., Federman, S. R., et al. 2007, *ApJ*, 667, 1002  
 Sipilä, O., Colzi, L., Roueff, E., et al. 2023, *A&A*, 678, A120  
 Stahl, O., Casassus, S., & Wilson, T. 2008, *A&A*, 477, 865  
 Taniguchi, K., Saito, M. & Ozeki, H. 2016, *ApJ*, 830, 106  
 Taniguchi, K., Ozeki, H., & Saito, M. 2017, *ApJ*, 846, 46  
 Tercero, F., López-Pérez, J. A., Gallego, et al. 2021, *A&A*, 645, A37  
 Tercero, B., Marcelino, N., Agúndez, M. et al. *A&A*, accepted  
 Vastel, C., Kawaguchi, K., Quénard, D. et al. 2018, *MNRAS*, 474, L76  
 Wakelam, V., Herbst, E., Loison, J.-C. et al. 2012, *ApJS*, 199, 21  
 Wilson, T. L. 1999, *Rep. Prog. Phys.*, 62, 143  
 Yan, Y. T., Henkel, C., Kobayashi, C. et al. 2023, *A&A*, 670, A98  
 Yoshida, K., Sakai, N., Nishimura, Y., et al. 2019, *PASJ*, 71, S18

## Appendix A: Line parameters

Line parameters for all observed transitions were derived by fitting a Gaussian line profile to them using the GILDAS package. A velocity range of  $\pm 20 \text{ km s}^{-1}$  around each feature was considered for the fit after a polynomial baseline was removed. Negative features produced in the folding of the frequency switching data were blanked before baseline removal. The derived line parameters for all observed lines are given in Table A.1. The  $J=4-3$  and  $J=5-4$  lines of HCCNC are shown in Fig. 1 and those of HNCCC in Fig. 2. The  $J=8-7$  to  $J=11-10$  lines of HCCNC and HNCCC are shown in Fig. A.1.

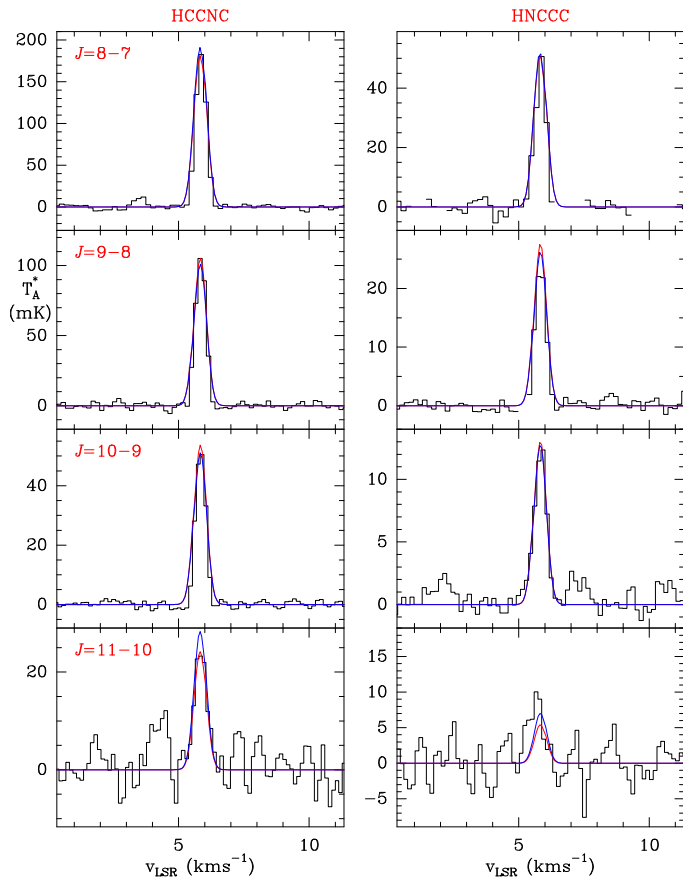


**Fig. A.1.** Observed lines in the 3mm domain of HCCNC (left panels) and HNCCC (right panels). The abscissa and ordinate are those of Fig. 1. The computed synthetic spectra adopting a constant rotational temperature are shown in red, whereas those obtained from the LVG model are shown in blue (see Sect. 3.3). The derived line parameters are given in Table A.1.

**Table A.1.** Observed line parameters for the isotopologs of HCCNC and HNCCC

Isotopolog	$J' - J''$	$F' - F''$	$\nu_{rest}^a$ (MHz)	$\int T_A^* dv^b$ (mK km s <sup>-1</sup> )	$v_{LSR}$ (km s <sup>-1</sup> )	$\Delta v^c$ (km s <sup>-1</sup> )	$T_A^{*d}$ (mK)
HCCNC	4-3	3-3	39742.141±0.010	3.46±0.06	5.83	0.63±0.01	5.20±0.08
		Main	39742.551±0.010	158.68±0.06	5.83	0.66±0.01	225.26±0.08
		4-4	39742.854±0.010	4.17±0.07	5.83	0.76±0.02	5.15±0.08
	5-4	4-4	49677.692±0.010	1.70±0.18	5.83	0.52±0.06	3.05±0.35
		Main	49678.073±0.010	133.98±0.16	5.83	0.57±0.01	220.85±0.35
		5-5	49678.380±0.010	1.79±0.19	5.83	0.61±0.07	2.76±0.35
	8-7		79484.128±0.002	98.19±1.20	5.81±0.01	0.50±0.01	186.30±2.12
	9-8		89419.261±0.002	55.74±0.88	5.82±0.01	0.48±0.01	109.13±2.10
	10-9		99354.258±0.002	26.27±0.40	5.82±0.01	0.46±0.01	53.66±0.99
	11-10		109289.104±0.002	15.40±1.58	5.81±0.03	0.59±0.07	24.25±3.46
H <sup>13</sup> CCNC	4-3		38504.814±0.010	1.82±0.14	5.83	0.69±0.06	2.47±0.10
	5-4		48130.904±0.010	1.63±0.12	5.83	0.56±0.05	2.73±0.17
HC <sup>13</sup> CNC	4-3		39595.414±0.010	1.97±0.08	5.83	0.63±0.03	2.95±0.11
	5-4		49494.159±0.010	1.50±0.17	5.83	0.53±0.07	2.67±0.25
HCCN <sup>13</sup> C	4-3		38438.852±0.010	1.72±0.10	5.83	0.65±0.04	2.49±0.10
	5-4		48048.456±0.010	1.08±0.11	5.83	0.46±0.05	2.21±0.17
HCC <sup>15</sup> NC	4-3		39557.774±0.010	0.85±0.10	5.83	0.81±0.10	9.94±0.13
	5-4		49447.148±0.010	0.73±0.11	5.83	0.70±0.11	9.85±0.20
DCCNC	4-3		36786.179±0.001	3.93±0.12	5.83±0.01	0.68±0.02	5.40±0.16
	5-4		45982.631±0.001	4.62±0.10	5.84±0.01	0.56±0.01	7.71±0.15
HNCCC	4-3	3-3	37346.067±0.010	2.16±0.07	5.83	0.69±0.02	2.94±0.09
		Main	37346.541±0.010	88.04±0.07	5.83	0.72±0.01	114.52±0.09
		4-4	37346.902±0.010	1.91±0.02	5.83	0.62±0.02	2.88±0.09
	5-4	4-4	46682.600±0.010	1.39±0.13	5.83	0.98±0.12	1.33±0.15
		Main	46683.063±0.010	69.54±0.14	5.83	0.61±0.01	107.31±0.15
		5-5	46683.435±0.010	1.17±0.15	5.83	0.68±0.10	1.63±0.15
	8-7		74692.130±0.010	28.86±2.19	5.83	0.52±0.05	51.93±4.08
	9-8		84028.265±0.010	12.71±0.37	5.83	0.49±0.02	24.22±0.75
	10-9		93364.268±0.010	7.53±0.38	5.83	0.57±0.03	12.40±0.74
	11-10		102700.117±0.001	6.43±1.39	6.03±0.07	0.67±0.16	9.10±3.06
HN <sup>13</sup> CCC	4-3		37245.805±0.010	0.87±0.08	5.83	0.65±0.07	1.26±0.09
	5-4		46557.148±0.010	1.04±0.14	5.83	0.71±0.09	1.69±0.22 <sup>e</sup>
HNC <sup>13</sup> CC	4-3		37148.515±0.010	1.00±0.07	5.83	0.72±0.06	1.31±0.07
	5-4		46435.534±0.010	0.91±0.12	5.83	0.64±0.10	1.32±0.17
HNCC <sup>13</sup> C	4-3		36007.309±0.010	1.66±0.07	5.83	1.11±0.05	1.40±0.07
	5-4		45009.056±0.010	1.10±0.11	5.83	0.74±0.08	1.40±0.14
DNCCC	4-3		35204.594±0.010	1.60±0.07	5.83	0.70±0.04	2.26±0.08 <sup>e</sup>
	5-4		44005.628±0.010	1.23±0.10	5.83	0.54±0.05	2.13±0.14

**Notes.** <sup>(a)</sup> Predicted or observed frequencies for the transitions of HCCNC and HNCCC and their isotopologs (see Sections 3.1 and 3.2). The observed frequencies have an uncertainty of 10 kHz and have been derived adopting a  $v_{LSR}$  of 5.83 km s<sup>-1</sup> (Cernicharo et al., 2020). The term *Main* refers to the  $\Delta F=+1$  transitions with  $F_u = J, J+1, J-1$  which are at nearly the same frequency and unresolved in our data. <sup>(b)</sup> Integrated line intensity in mK km s<sup>-1</sup>. <sup>(c)</sup> Line width at half intensity using a Gaussian fit in the line profile (in km s<sup>-1</sup>). <sup>(d)</sup> Antenna temperature (in mK). <sup>(e)</sup> Data only come from the set of observations with frequency throw of 10 MHz.